Compositional and orientational control in metal halide perovskites of reduced dimensionality

Rafael Quintero-Bermudez[1], Aryeh Gold-Parker[2,3], Andrew H. Proppe[1,4], Rahim Munir[5], Zhenyu Yang[1], Shana O. Kelley[4,6], Aram Amassian[5], Michael F. Toney[2] and Edward H. Sargent[1]*

Reduced-dimensional metal halide perovskites (RDPs) have attracted significant attention in recent years due to their promising light harvesting and emissive properties. We sought to increase the systematic understanding of how RDPs are formed. Here we report that layered intermediate complexes formed with the solvent provide a scaffold that facilitates the nucleation and growth of RDPs during annealing, as observed via in situ X-ray scattering. Transient absorption spectroscopy of RDP single crystals and films enables the identification of the distribution of quantum well thicknesses. These insights allow us to develop a kinetic model of RDP formation that accounts for the experimentally observed size distribution of wells. RDPs exhibit a thickness distribution (with sizes that extend above $n = 5$) determined largely by the stoichiometric proportion between the intercalating cation and solvent complexes. The results indicate a means to control the distribution, composition and orientation of RDPs via the selection of the intercalating cation, the solvent and the deposition technique.

Metal halide perovskites have attracted extensive interest in recent years due to their ease of fabrication, high charge-carrier mobilities and low density of deep electronic trap states[1–3]. Perovskite materials have achieved a superior performance in photovoltaics (PVs)[4–6] and light-emitting devices[7,8] and are enabling advances in next-generation optoelectronic devices[9]. To improve the long-term operational stability of these promising materials has therefore become a priority[10–13].

Reduced-dimensional (2D and quasi-2D) metal halide perovskites (RDPs)[14,15], synthesized with the addition of large intercalating cations (such as phenethylammonium (PEA)[16–18] and *n*-butylammonium (BTA)[19]), have attracted attention as a means to address long-term stability[20]. In such materials, perovskite layers are separated by bilayers of organic cations that are ionically bonded to halide groups in the perovskite. The halide-rich surfaces at the perovskite grain boundaries are better protected from oxidation and degradation in RDPs, which leads to an enhanced stability[17]. RDPs have also proven exceptional for light-emitting applications, which led to record-performing devices[16,21]. The crystal system exhibits the $R_2A_{n-1}B_nX_{3n+1}$ structure in which R is the intercalating cation and *n* represents the number of perovskite layers in a well. This notation can also be used to represent 3D (n → ∞), 2D ($n = 1$) and quasi-2D ($n > 1$)[16–18,22,23] (Fig. 1a).

Grazing-incidence X-ray scattering techniques are used to study 3D perovskite materials. Much has been achieved in determining film morphology, grain sizes and crystal orientation[24]. These techniques are applied to RDPs[18,19,23], but to obtain a detailed understanding of the nature of films, such as well-thickness distribution and orientation, is not yet fully developed. These structural properties can have important consequences to device performance due to their effects on the energy landscape homogeneity and anisotropic charge transport along different directions of the RDPs. Furthermore, conclusive evidence remains to

be found as to the possibility of the formation of large *n* ($n > 5$) quasi-2D quantum wells (QWs)[17,22]. We make use of these techniques, accompanied by photophysical and topographical measurements, to increase our understanding of the physical and chemical composition of RDP films.

The mechanism by which these materials assemble also remains to be understood. Herein we undertake studies of the kinetics of film formation as well as the state of the resulting materials. The results of this study indicate that the deposition technique, intercalating ligand, stoichiometry of the precursors and solvent can each vary the QW orientation and thickness distribution systematically, which enables a level of control for future RDP-based devices.

We focus on methylammonium (MA) lead iodide RDPs with PEA and BTA as the large intercalating cation, but also discuss the generality of our findings. We use the value *n* to identify the number of perovskite layers in a single well, whereas ⟨n⟩ identifies the average number of perovskite layers per well in a film.

QW distribution

We first investigated the crystallinity of films using X-ray diffraction (XRD). Ordered QWs of varying thicknesses can be readily distinguished from the analysis of the small-angle domain of XRD patterns. The XRD pattern of QWs of various sizes was simulated to facilitate this analysis (Fig. 1b)[25,26]. The strongest diffraction peak of RDPs corresponds to their (001) diffraction. In PEA–MAPbI₃, for instance, this corresponds to *d* spacings of 1.66–7.40 nm for wells of thickness $n = 1$–10. Grazing-incidence small-angle X-ray scattering (GISAXS) measurements (Supplementary Fig. 26) were performed on films of various ⟨n⟩ values to determine the distribution of QW thicknesses. The integrated GISAXS data (Fig. 1c) can be compared to the theoretical small-angle XRD pattern (Fig. 1d) to identify the presence of particular crystal grains. Ordered domains of $n = 1$, 2 and 3 can be identified in varying proportions for samples

[1]Department of Electrical and Computer Engineering, University of Toronto, Toronto, Ontario, Canada. [2]SLAC National Accelerator Laboratory, Menlo Park, CA, USA. [3]Stanford University Department of Chemistry, Stanford, CA, USA. [4]Department of Chemistry, University of Toronto, Toronto, Ontario, Canada. [5]King Abdullah University of Science and Technology (KAUST), KAUST Solar Center (KSC), and Physical Sciences and Engineering Division, Thuwal, Saudi Arabia. [6]Department of Pharmaceutical Sciences, Leslie Dan Faculty of Pharmacy, University of Toronto, Toronto, Ontario, Canada. *e-mail: ted.sargent@utoronto.ca
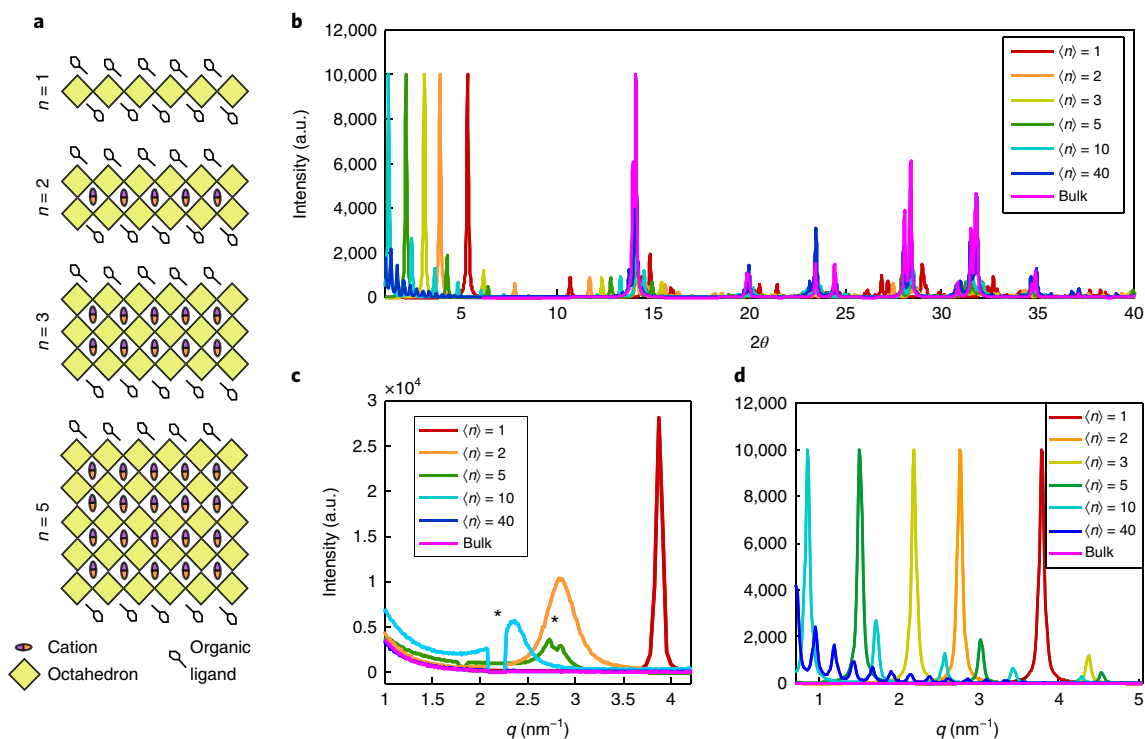
Fig. 1 | Structure and diffraction of RDPs. a, General schematic representation of RDPs. **b**, Simulated powder XRD of pure $PEA_2MA_{n-1}Pb_nI_{3n+1}$ wells show the clearest distinctive features in the small-angle domain due to (001) RDP reflections. **c**, Cuts along the q_z axis of experimental GISAXS measurements on real samples show distinct features that reveal a mixed population of RDP thicknesses (asterisks identify spaces between detectors). **d**, These peaks can be labelled via theoretical GISAXS patterns for pure wells.

of $\langle n \rangle = 2$, 5 and 10, but no distinct peaks for ordered regions $n > 3$ can be discerned.

The lack of distinct small-angle XRD peaks for ordered regions with $n > 3$ (Fig. 1c) does not preclude the existence of $n > 3$ wells; instead, it indicates merely that sufficiently coherent crystallographic regions with $n > 3$ are not present (Supplementary Information). Interestingly, however, in samples with $\langle n \rangle = 5$ and 10, scattering below $2\,nm^{-1}$ was observed compared to the baseline in the bulk sample, which suggests incoherent large QWs. In addition, the asymmetry of the $n = 3$ peak in the $\langle n \rangle = 5$ sample suggests the presence of larger QWs, perhaps $n = 4$. To determine the distribution of QWs in the films, we made use of ultrafast transient absorption (TA) spectroscopy.

Due to the quantum confinement in RDPs, the bandgap of the material increases as the thickness of the QW decreases. With an exciton Bohr radius of 25 Å (ref. [27]), a strong dependence of the bandgap energy on the QW thickness is expected for QWs with up to five perovskite layers, and only small shifts in the bandgap energy thereafter. To understand the observed TA spectra of RDPs, we also analysed single crystals[28]. TA spectra were acquired for these crystals, which allowed us to identify the distinctive bleach peaks for single crystals of $n = 2$, 3 and 4 (Fig. 2a–c). Although these crystals are predominantly pure phase, it is nonetheless possible to identify regions of crystals with multiple QW thicknesses (Fig. 2d). TA spectra on RDP films (Fig. 2e–p, and Supplementary Figs. 15–19 and 23), in contrast, illustrate the large distribution in QWs that is not discernible in GISAXS.

In the series of spin-cast and hot-cast RDP films, distinct peaks are seen for QWs of $n < 6$ (Fig. 2e–2i), and a separate bulk peak can also be identified (Fig. 2k). Large $\langle n \rangle$ quasi-2D samples exhibit distinctive bleach features between those of $n = 5$ and bulk, which indicates the formation of wells with large n values (Fig. 2f–2j). This TA feature for large n redshifts further for samples of increasing $\langle n \rangle$, which suggests an increase in the average QW thickness.

To estimate the distribution of QW sizes indicated using TA spectral features, we sought to determine the bandgap dependence on well thickness. We followed a procedure corroborated by both empirical fitting[29] (validated by data collected in this work and previous literature[22,30,31]) and an effective-mass-approximation model[32] (Supplementary Information). The predicted TA bleach wavelength was obtained by adding a blueshift (which results from exciton–exciton interactions[30] and the Moss–Burstein effect[33] in narrow wells and larger bulk-like wells, respectively) to the calculated bandgap value (Fig. 2l). The TA spectra were then fit to model the bleach peak of the QWs of varying thicknesses with the bandgaps estimated in Fig. 2l (Supplementary Information), and the data are presented through histograms in the insets of Fig. 2f–j. These allow the determination of the QW thicknesses exhibited in an RDP film, but do not directly represent the QW thickness distribution. There are two reasons for this: (1) the oscillator strength for QWs varies as a function of the n value, and is expected to increase as QW thickness decreases; (2) the positive feature (redshifted relative to the main bleach peak) identified in pure single crystals inhibits the total bleach observed for the next-highest n-valued QW in the films. These effects are expected to lead to a higher measured bleach intensity for low-n QWs, in particular $n = 2$.

The TA bleach fitting demonstrated a QW distribution peaked around $\langle n \rangle$ with a standard deviation that increases with $\langle n \rangle$. For instance, among the PEA-based spin-cast films (Fig. 2e–k), sample $\langle n \rangle = 2$ is made up of QWs with $n = 1$, 2 and 3; $\langle n \rangle = 3$ exhibits $n = 1$–10, $\langle n \rangle = 5$ exhibits $n = 2$–15 and $\langle n \rangle = 10$ is made up of predominantly $n = 3$–20. Even the $\langle n \rangle = 40$ sample exhibits a bleach with a 6 nm blueshift with respect to the bulk feature, which evidences some degree of quantum confinement. This sample is made up of very large wells ($n > 20$), and fitting reveals a small percentage of wells with an ultralarge n ($n > 40$) that are energetically indistinguishable from bulk. By measuring spectra of both the front and
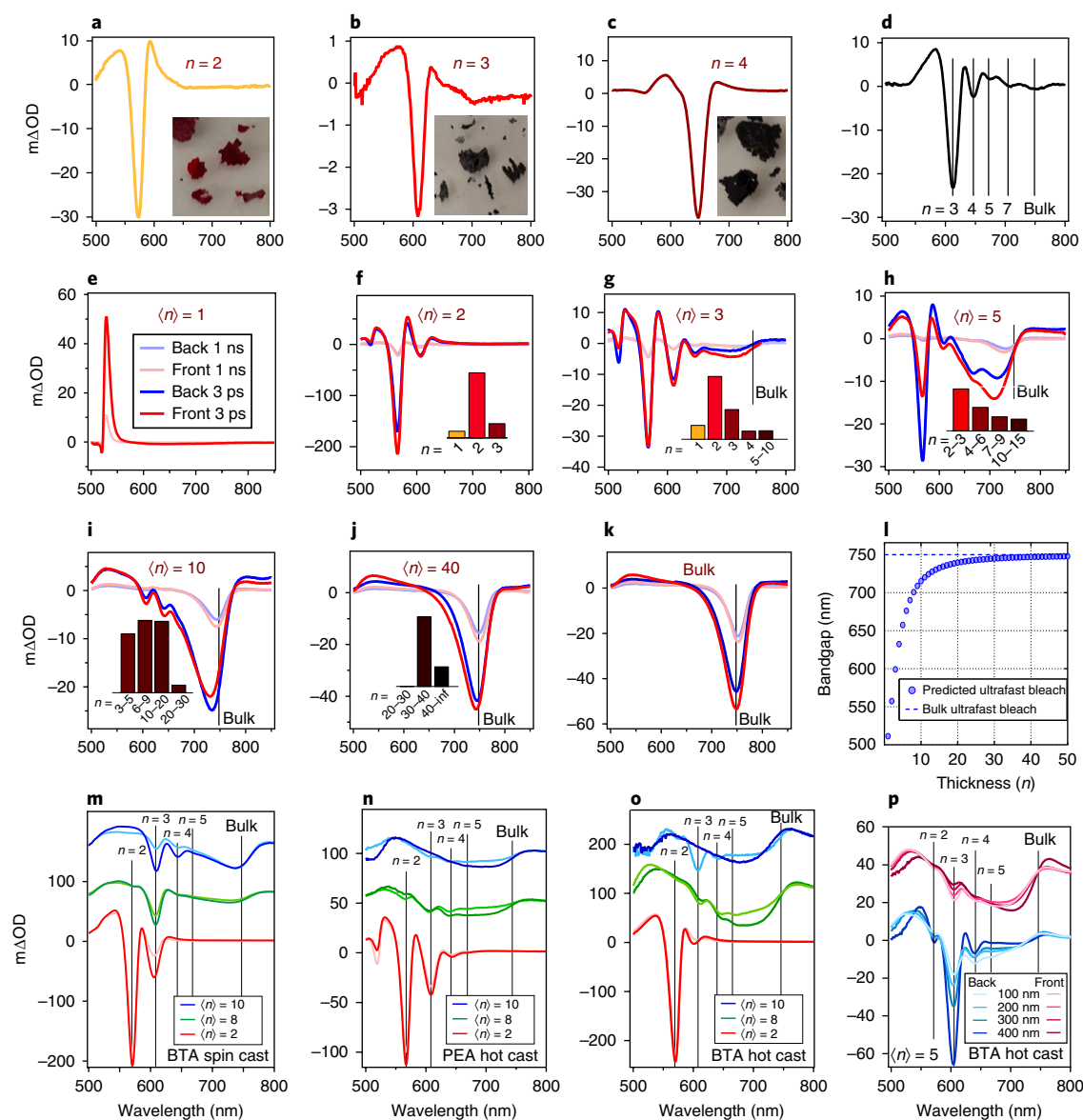
Fig. 2 | Ultrafast TA spectra of RDPs. a–d, TA spectra of layered single crystals of $n = 2$ (**a**), 3 (**b**) and 4 (**c**) and a segment that exhibits clear $n = 3-7$ exemplify the ultrafast spectra for pure phases. **e–k**, TA spectra of spin-cast PEA-based samples of $\langle n \rangle = 1$ (**e**), 2 (**f**), 3 (**g**), 5 (**h**), 10 (**i**), 40 (**j**) and bulk (**k**) reveal that the broad distribution of QW thicknesses extends well beyond $n = 5$. TA on the front and back sides of the films indicate a higher concentration of thin wells at the top of the films. The TA spectra change dramatically after a few picoseconds due to carrier funnelling into thicker wells. **l**, The predicted TA bleach for QWs of size n enables the labelling of RDP thicknesses and fitting of the ultrafast spectra, which enable the identification of the distribution of bleach intensities (histograms in **f–j**). **m–o**, TA spectra for spin-cast BTA-based (**m**), hot-cast PEA-based (**n**) and hot-cast BTA-based (**o**) RDPs reveal the control of well distribution effectuated by variations in the large cation and film synthesis. **p**, The accentuated grading distribution effect imposed by increasing the film thickness in hot-cast films.

the back of the film, we ascertained differences in the populations between the top and bottom of the film[22]. We observed a predominantly higher concentration of low-n wells at the top of the film, as discussed in the next section.

The BTA-based spin-cast RDPs exhibit quite similar spectra to those of their PEA-based counterparts. However, features with a low n are enhanced in the former (Fig. 2m). Additionally, the large n feature is concurrently redshifted in the BTA-based series, as expected due to the depleted organic ligand. Hot casting dramatically changes the distribution of RDPs (Fig. 2n–p). First, a stark contrast is observed between the front and back of the film, which indicates an inhomogeneous distribution of QWs with a higher concentration of large n wells near the surface of the film and low n wells at the bottom. This contrast is further pronounced as the thickness

of the film increases (Fig. 2p and Supplementary Figs. 15 and 16). Second, the distribution of QWs is more sharply centred at $\langle n \rangle$ in hot-cast films. To determine the causes for variations in the QW distribution, we investigated their formation mechanisms further in the studies described next.

Formation kinetics

We sought to determine the mechanism of RDP formation by investigating the evolution of grazing-incidence X-ray scattering during film deposition. Along the planes of semiconductor wells, charge-carrier mobility is comparable to that of bulk perovskite; normal to these planes, however, the large organic bilayer severely hinders charge transport. To capture the diffraction peaks that could distinguish the perovskites from the precursors, we used in situ
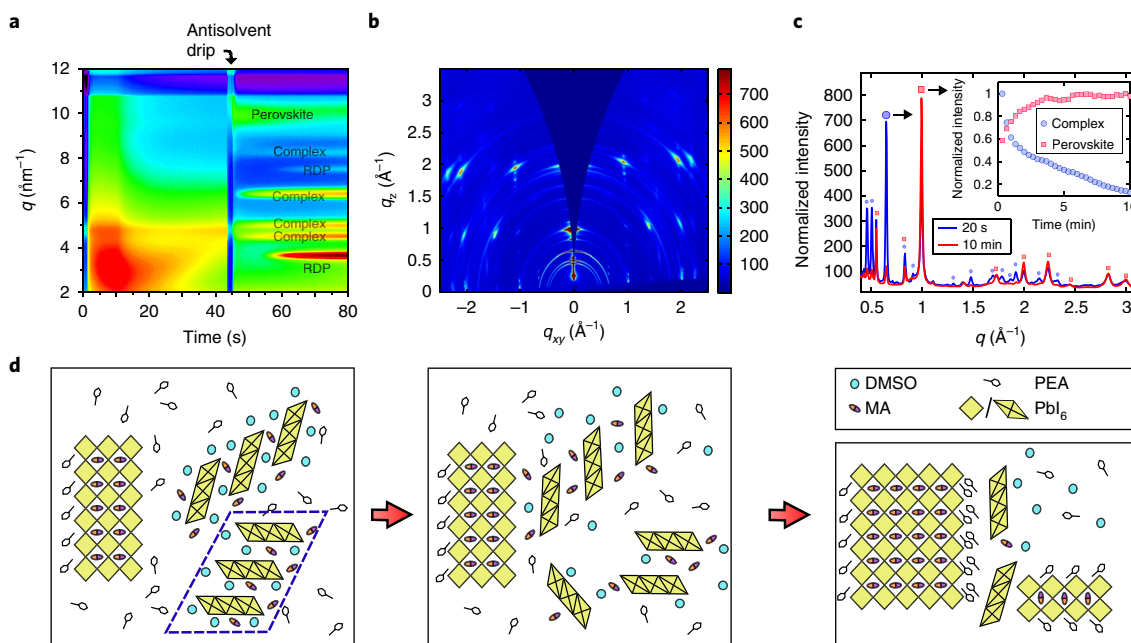
Fig. 3 | Formation kinetics of RDPs via in situ GIWAXS. a, The X-ray scattering evolution during the film spinning process highlights the formation of an intermediate phase after the antisolvent drip. **b,c**, Measured GIWAXS pattern after spinning and before the annealing process (**b**) and the azimuthally integrated GIWAXS data for ⟨n⟩ = 10 film during the annealing (**c**) demonstrate the formation of solvent complexes and their evolution. The evolution of the amplitudes of the DMSO complex and RDP peaks after fitting over time reveal the mechanism for RDP formation (inset). **d**, These studies indicate the formation of solvent complexes (blue segmented rhomboid), which disintegrate partially to provide a framework for the nucleation (bottom right at each stage) and growth (left/top) of the RDPs during the annealing process. The dissolved large cations in the film (PEA in this case) form organic bilayers in the growth process when there is a sufficient amount present.

grazing-incidence wide-angle X-ray scattering (GIWAXS). We discuss first the use of dimethylsulfoxide (DMSO) as the solvent, and then the effect of varying the solvents.

On spin casting the precursor solution, we observe a broad low-angle scattering consistent with a colloidal precursor–sol-gel (Fig. 3a). After the antisolvent drip, the features change abruptly, which leads to broad diffraction peaks (for example, $q = 0.65 \text{Å}^{-1}$ at 45 s) that do not belong to either the perovskite or the precursor compounds. Similar diffraction patterns have been observed before in 3D perovskites, where such patterns were attributed to intermediate crystalline complexes made up of perovskite precursors and solvent molecules[34–36]. Scattering consistent with this intermediate phase appears after the antisolvent drip and intensifies during spin coating, which evidences the formation of the solvent complex phase during spin coating. Seconds after the drip, some perovskite diffraction begins to appear. At the end of the spin coating, the film exhibits predominantly solvent complexes that coexist with some RDP diffraction (Fig. 3b).

A more dramatic transformation is observed as the film is annealed (Fig. 3c and Supplementary Videos 1 and 2). During this process, GIWAXS clearly depicts the emergence of perovskite peaks with a commensurate subsidence of the intermediate solvent complex peaks over the course of ten minutes of annealing (Fig. 3c and Supplementary Figures 11–13). Furthermore, the intermediate complex peaks, unlike those of RDPs, exhibit nearly anisotropic ring patterns.

We analysed the intensity of the perovskite and intermediate solvent complex peaks over time during the annealing process to study the kinetics of the RDP formation. Interestingly, the rate of subsidence of solvent complex peaks mirrors the rate of perovskite peak emergence, which shows a direct transition from the solvent complex to the RDP. The same analysis performed on different ⟨n⟩ RDP samples and bulk perovskite showed similar trends, which

suggests similar growth mechanisms. The rates of evolution may differ due to increases in the enthalpy of formation for RDPs of decreasing thickness[17].

The evolution of the scattered intensity illustrates the formation kinetics of the RDPs (Fig. 3d). After the deposition of the precursor solution by spin casting, the resulting film is made up of largely unoriented intermediate solvent-precursor complexes (ring patterns in Fig. 3b) among the dissolved large cations. This point is evidenced by the lack of crystalline cation (in this case, PEA iodide) peaks and the fact that the solvent complex diffraction pattern is identical to the complex for bulk perovskite formation, in which the large cation is not present (Supplementary Fig. 14). Previous reports found that the large solvent complexes slowed down the reaction between the perovskite precursors, which ultimately led to larger and more uniform bulk perovskite grains[34]. In 2D and quasi-2D perovskites, however, the large solvent complexes provide a framework that may facilitate the construction of perovskite QWs. The results further suggest that, as the film is annealed, solvent molecules begin to weaken the complex as they evaporate out, which allows newly released PbI₂ layers, methylammonium iodide and partially formed complexes to nucleate and grow RDP grains. It was concluded in bulk perovskite studies that the expanded lattice of solvent complexes could allow reagents to enter[37], which could facilitate the nucleation of organic bilayers in RDP films. During this process, half-formed complexes and PbI₂ layers could realign amid the solvent and dissolved cation. This is evidenced by the fact that intermediate crystalline solvent complexes are predominantly unoriented, but as these grow existing grains they align with the rest of the RDP crystallites. By the end of the annealing process, all the solvent complex has been completely replaced by RDP.

The RDP formation characterized in this study agrees with prior work that studied 2D nanocrystal formation of different materials. Previous studies found that, unlike the formation of
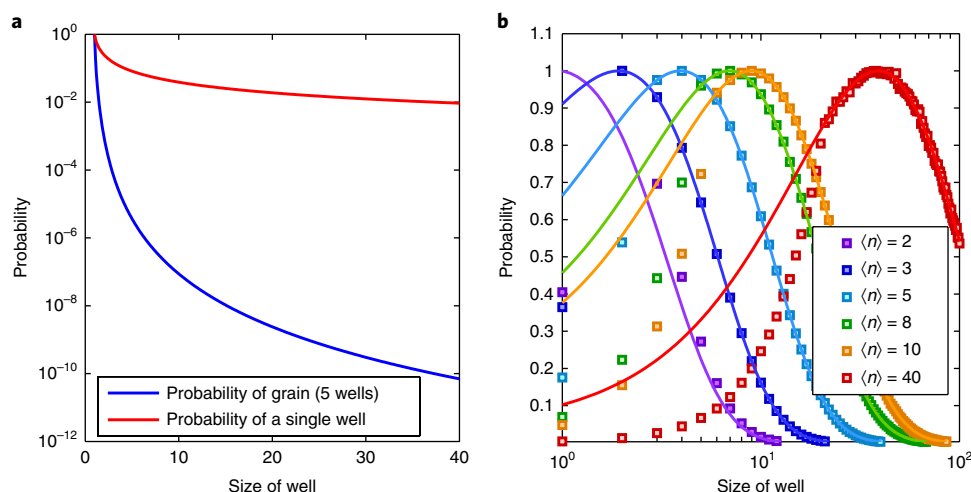
Fig. 4 | Statistical model of the formation of RDPs. a, The theoretical probability of forming a single well or a single grain (defined as five consecutive wells) of size x in sample $\langle x \rangle$ was computed analytically for the growth model identified assuming a uniform and constant distribution of the large organic cation. **b**, The population distribution of well thicknesses was computed analytically by the model (continuous) and simulated via Monte Carlo to take into account variations in the large organic cation distribution throughout the growth process (squares). The theoretical skew log-normal and symmetric log-normal distributions of well thicknesses centred at $\langle n \rangle$ were ascertained for the analytical and Monte Carlo models, respectively, and agreed well with the distributions measured via TA.

layered crystal structures (for example, MoS_2), the formation of 2D and quasi-2D nanostructures for non-layered systems (for example, wurtzite and zinc blende) is mediated by a layered meso-phase made up of precursors and solvents[38–40]. These nanosheets provide a template for 2D nanostructure nucleation and growth. These mesophases are, in turn, facilitated by the use of layered precursors, such as $CdCl_2$ and CdI_2 (refs [38,41]). RDP formation follows a similar pathway. In this case, however, a low activation energy for RDP growth could allow RDPs to form rapidly in the film during the annealing process[37].

With the aid of the formation kinetics model (Fig. 3d), we can determine the probability distribution of wells. The ratio of large cations to the intermediate solvent complexes is the defining parameter in the model. Statistics of well formation are computed analytically and by a Monte Carlo simulation (Supplementary Information).

We first computed the probability of forming a single well of size n (in a given film $\langle n \rangle$) and compared it to the probability of forming a highly crystalline domain with well size n that would exhibit a distinct XRD signal (Fig. 4a). This analysis found that it is drastically less probable to form an entire domain of a given well thickness than it is to form a single well. Furthermore, this probability decreases significantly with well size such that an entire grain of $n > 5$ is highly unlikely. This finding reconciles the results from GISAXS (Fig. 1c) and TA (Fig. 2) such that, despite the abundant presence of large QWs, a poor spatial coherence for large QWs leads to broad weak diffraction peaks that merge together, as observed in the scattering $< 2\,nm^{-1}$.

The calculations exhibit a log-normal well-thickness distribution, which denotes a tighter standard deviation for low-n wells than for large-n wells. This result agrees well with all the other measurements, with one exception. Large bleach peaks for low-n wells were observed in TA that did not follow the log-normal distribution. Variations in oscillator strength are the likely culprit (Supplementary Fig. 24 and Supplementary Table 1). An inhomogeneous distribution of the dissolved large cation throughout the film could also distort the distribution, albeit to a lower degree. Furthermore, the latter could also explain the variations across the thickness of the film.

Orientation

Our series of measurements shows that the orientation of wells depends primarily on the QW thickness (Fig. 5a–m and Supplementary Fig. 10). QWs with smaller n values are more likely to orient parallel to the substrate, whereas thicker wells ($n > 4$) preferentially orient normal to it. We observed this behaviour to vary gradually as n increases: sample $\langle n \rangle = 1$ yields entirely horizontally lying wells, samples whereas $2 \le \langle n \rangle \le 4$ exhibit fewer horizontal and increasingly more vertically standing wells. Hot-cast films exhibit similar trends, but also showed a dramatic reduction in the presence of anisotropic rings, which indicates a reduced presence of randomly oriented wells. Both horizontal and vertical wells were identified in these measurements. Additionally, the thickness of the film was found to have an effect on the orientation of wells: in thin samples of similar precursor ratios, the horizontally lying wells far outnumber the vertically standing wells (Supplementary Fig. 12).

These observations agree well with nucleation–growth theory and experimental studies in other 2D nanostructures. Previous work found a substantial energetic barrier in starting a new monolayer in 2D crystals but, once nucleated, lateral crystal growth proceeds quite rapidly[38,41]. In RDPs, the precursors are released from their solvent complexes during thermal annealing; these will begin to nucleate monolayers, which will grow to certain thicknesses before forming organic bilayers that depend on the stoichiometry. The orientation of the RDPs could be explained by the varying rates of precursor availability for vertically standing vis-à-vis horizontally lying wells due to the normal-oriented solvent evaporation. Growth can, however, be cut off depending on the dimensions of the film; a thin film hinders the growth of vertically standing wells. This growth model agrees with previous work that found spin-cast perovskite films undergo a homogeneous nucleation[42]. A similar orientation has been observed in other 2D nanostructures[43,44]. The studies in this work were also repeated for different substrates, which showed the same trends (Supplementary Figs. 10 and 25). The morphology of the films was also corroborated by means of topographic atomic force microscopy (AFM) (Supplementary Fig. 21).

The TA and GIWAXS measurements on hot-cast films exhibit some differences compared to those on spin-cast films. The hot temperature of the substrate in the hot technique would speed up
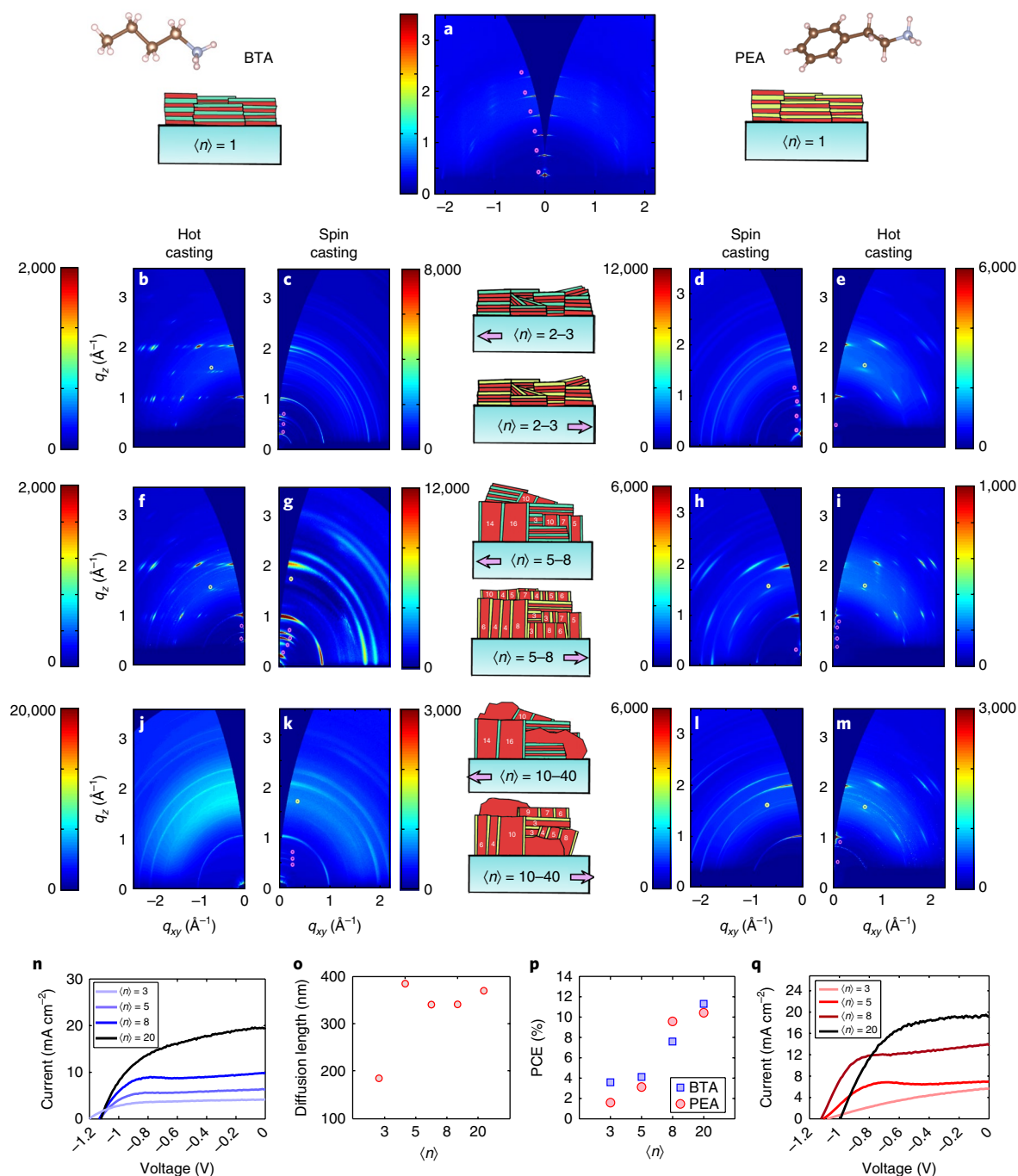
Fig. 5 | Orientational analysis of RDPs. a–m, GIWAXS measurements of hot-cast and spin-cast BTA-based (**b**, **c**, **f**, **g**, **j** and **k**) and PEA-based RDPs (**a**, **d**, **e**, **h**, **l** and **m**) in four different size regimes, which, along with all the other characterizations performed, enable a generalized concept of the QW morphology in both the PEA-based and the BTA-based spin-cast films (central column). Pink and yellow circles highlight features that identify parallel-lying and perpendicular-standing RDPs, respectively. **n–p**, *J–V* curves of the PV devices composed of BTA-based RDPs (**n**) and PEA-based RDPs (**q**), as well as their diffusion lengths (**o**) and power conversion efficiencies (PCE) (**p**), illustrate the effect of morphology on device performance.

the transformation from intermediate complexes to RDPs. The rapid transformation could consume the large organic cation in the lower part of the film to leave a lower concentration for the rest of the film, which would explain the gradient in well thicknesses observed here and in previous literature[22], particularly in thicker films. We also observed that hot-cast films exhibit higher degrees of preferential orientation than spin-cast films. This may be due to a change in surface energetics or the fast rate of solvent evaporation. Recent studies on the nucleation of RDPs via hot casting found that

the hot temperature on one side of the film could alter the nucleation mechanism, which leads to a heterogeneous nucleation[45]. As found in previous work, preferential heterogeneous nucleation could lead to such differences in orientation. This could also explain our observations in well-thickness distribution.

Among spin-cast films, we identified four different types of film formation for RDPs (Fig. 5). Films of $\langle n \rangle = 1$ form parallel-aligned pure $\langle n \rangle = 1$ wells. Films of $\langle n \rangle = 2–4$ are fairly monodisperse, but with more mixing and more random orientation, albeit still

a preferential tendency to align parallel to the substrate. Films of $\langle n \rangle = 5$–10 tend to form primarily large wells perpendicular to the substrate, but QWs with small n values parallel to the substrate can still be observed. Finally, films of $\langle n \rangle \geq 10$ still show a preferential orientation for large-n wells to align normal to the surface, but with the addition of the anisotropic bulk-like grains. In this class, PEA RDPs no longer exhibit small-n wells, whereas BTA RDPs still do. This could be attributed to the smaller and less bulky nature of BTA which redistributes more readily than PEA within the solvent, and so enables a higher probability of forming low-n wells. Furthermore, the preferred orientation on the BTA films is less pronounced among categories 3 and 4.

Multiple examples for each class were studied (Supplementary Information). An in-depth orientation analysis of GIWAXS patterns is provided in Supplementary Figs. 2–5), by which key XRD peaks are identified that distinguish parallel- and perpendicular-oriented wells. These key features are indicated by pink and yellow circles denoting parallel- and perpendicular-oriented wells (Fig. 5), respectively. Notably, as thick wells do not exhibit (001) reflections discernible from the bulk, the tetragonal perovskite unit cell within layers is used to determine the orientation of the RDPs.

Device implications

We constructed PV devices with the films analysed (Fig. 5n–q) to identify key morphological properties. We also measured diffusion lengths (Fig. 5o) for a range of RDP films (Supplementary Table 2)[46]. We find that films with more vertically aligned wells ($\langle n \rangle > 4$) exhibit much longer diffusion lengths, comparable to that of bulk perovskite. This is probably due to a decreased occurrence of horizontal wells and randomly oriented crystal grains.

We identified three main RDP film properties that affect PV devices (Fig. 5n,q): orientational disorder, energetic disorder and inefficient light absorption. (1) QW orientational disorder and the prevalence of horizontal wells, particularly among low-$\langle n \rangle$ films, can be identified as a source of resistive losses in the device, which limits the fill factor. (2) The bandgap distribution in RDPs leads to voltage losses in PV devices. Bandgap is increased in low-$\langle n \rangle$ films, and as such the open-circuit voltage is expected to increase. However, the open-circuit voltage is identical for most RDP samples. This voltage loss (particularly among mid-range $\langle n \rangle$ devices, for example, $\langle n \rangle = 5$) is mainly attributable to the QW polydispersity. In addition, the presence of low-n wells can act as traps for charge carriers due to the type-II band alignment of thin wells[47], an effect that leads to short-circuit current density losses. (3) As $\langle n \rangle$ decreases, so does the probability of generating photocarriers due to the decreased absorbance of films (Supplementary Fig. 28); this is probably caused by the reduced density of the perovskite in the RDP films as the proportion of organic ligands is increased. This issue could be addressed by increasing the film thickness and decreasing the organic ligand length.

Hysteresis in PV devices is also increased by the introduction of RDPs in PVs (Supplementary Fig. 29). Thin wells could act as shallow traps for holes, according to the band alignment found in previous work[47].

Discussion

In the kinetics study, we found that intermediate solvent complexes mediate the formation of wells by slowly providing building blocks to nucleate and grow RDPs as the solvent evaporates out, and thereby weakens the complexes. The RDP QW polydispersity is thus strongly dependent on the distribution of the large cation throughout the film. Therefore, a homogeneous distribution of large cations should lead to a log-normal distribution of wells centred near the expected $\langle n \rangle$ set by the precursor ratios. The kinetics of the formation of RDPs observed here can be applied generally to most $R_2A_{n-1}B_nX_{3n+1}$ layered structures in aprotic solvents, although the

distribution of well thicknesses and morphology is dependent on the solvent (for example, surface wettability) and the large organic cation properties (for example, solubility).

To study the effect of the solvent on growth and distribution, we undertook in situ GIWAXS measurements (Fig. 3) for various solvents (Supplementary Fig. 27 and Supplementary Videos 2–4). DMSO solutions exhibit the intermediate complexes, analysed in Fig. 3, that allowed the kinetic analysis. Dimethylformamide (DMF), another commonly used aprotic solvent, has been found to form solvent complexes in bulk perovskite as well, but due to its lower melting and boiling points, in certain conditions it annealed at room temperature[35,37]. As one might expect, no intermediate complexes were observed, probably due to the volatility of DMF. This probably leads to a faster growth kinetics that would hinder crystallinity and film quality. However, N-methyl-2-pyrrolidone solutions were found to yield a broad peak under $1\,\text{Å}^{-1}$, which disappeared during the annealing process. The weak and broad nature of the intermediate peak suggests disordered solvent–precursor complexes, which would explain the anisotropic orientation of the resulting films. The selection and ratio of the solvents were also found to modify the distribution of QWs (Supplementary Figs. 18 and 19). Increasing the concentration of DMSO and N-methyl-2-pyrrolidone was found to lead to a redshift in the QW distribution, whereas the concentration of DMF was found to lead to a blueshift. This arises from differences in the solubility of the large cation (BTA or PEA) in the different aprotic solvents. In sum, the solvent holds the key to controlling the rate of RDP formation which can ultimately enable the tunability of the QW distribution and crystallinity. Furthermore, the formation of precursor complexes in a given solvent also leads to variations in the QW orientation. Different solvents and combinations could enable further fine tuning of the RDP properties.

The present study also found that the choice of large cation and film deposition method led to variations in the QW distribution. Using BTA instead of PEA in RDPs leads to a higher concentration of low-n RDPs and a concurrent redshift of the large-n wells (Fig. 2). In addition, the selective reactivity between the various ions in the precursor solution and its modulation by varying the large organic cation could also affect the kinetic rates in RDP formation. Hot casting leads to a well-defined RDP orientation and QW thickness inhomogeneity: low-n wells tend to form at the bottom, whereas large-n wells congregate near the surface of the films.

In summary, our outcomes present a significant advance in understanding the formation and controlling the distribution, composition and orientation of RDPs by variations in the solvent, large cation and film deposition. This work paves the way towards engineering higher quality materials for more efficient and stable optoelectronic devices.

Methods

Methods, including statements of data availability and any associated accession codes and references, are available at https://doi.org/10.1038/s41563-018-0154-x.

References

1. Shi, D. et al. Low trap-state density and long carrier diffusion in organolead trihalide perovskite single crystals. *Science* **347**, 519–522 (2015).
2. Wehrenfennig, C., Eperon, G. E., Johnston, M. B., Snaith, H. J. & Herz, L. M. High charge carrier mobilities and lifetimes in organolead trihalide perovskites. *Adv. Mater.* **26**, 1584–1589 (2014).
3. Xing, G. et al. Long-range balanced electron- and hole-transport lengths in organic–inorganic CH₃NH₃PbI₃. *Science* **342**, 344–347 (2013).
4. Yang, W. S. et al. High-performance photovoltaic perovskite layers fabricated through intramolecular exchange. *Science* **348**, 1234–1237 (2015).

5. Bi, D. et al. Polymer-templated nucleation and crystal growth of perovskite films for solar cells with efficiency greater than 21%. *Nat. Energy* **1**, 16142 (2016).

6. Tan, H. et al. Efficient and stable solution-processed planar perovskite solar cells via contact passivation. *Science* **726**, 722–726 (2017).

7. Pan, J. et al. Highly efficient perovskite-quantum-dot light-emitting diodes by surface engineering. *Adv. Mater.* **28**, 8718–8725 (2016).

8. Yakunin, S. et al. Low-threshold amplified spontaneous emission and lasing from colloidal nanocrystals of caesium lead halide perovskites. *Nat. Commun.* **6**, 8056 (2015).

9. Sutherland, B. R. & Sargent, E. H. Perovskite photonic sources. *Nat. Photon.* **10**, 295–302 (2016).

10. Bryant, D. et al. Light and oxygen induced degradation limits the operational stability of methylammonium lead triiodide perovskite solar cells. *Energy Environ. Sci.* **9**, 1655–1660 (2016).

11. Yuan, Y. & Huang, J. Ion migration in organometal trihalide perovskite and its impact on photovoltaic efficiency and stability. *Acc. Chem. Res.* **49**, 286–293 (2016).

12. Berhe, T. A. et al. Organometal halide perovskite solar cells: degradation and stability. *Energy Environ. Sci.* **9**, 323–356 (2016).

13. Leo, K. Perovskite photovoltaics: Signs of stability. *Nat. Nanotech.* **10**, 574–575 (2015).

14. Mitzi, D. B. in *Progress in Inorganic Chemistry* Vol. 48 (ed. Karlin, K.D) 1–121 (Wiley, Hoboken, NJ, 1999).

15. Mitzi, D. B., Feild, C. A., Harrison, W. T. A. & Guloy, A. M. Conducting tin halides with a layered organic-based perovskite structure. *Nature* **369**, 467–469 (1994).

16. Yuan, M. et al. Perovskite energy funnels for efficient light-emitting diodes. *Nat. Nanotech.* **11**, 872–877 (2016).

17. Quan, L. N. et al. Ligand-stabilized reduced-dimensionality perovskites. *J. Am. Chem. Soc.* **138**, 2649–2655 (2016).

18. Byun, J. et al. Efficient visible quasi-2D perovskite light-emitting diodes. *Adv. Mater.* **28**, 7515–7520 (2016).

19. Tsai, H. et al. High-efficiency two-dimensional Ruddlesden–Popper perovskite solar cells. *Nature* **536**, 312–316 (2016).

20. Grancini, G. et al. One-year stable perovskite solar cells by 2D/3D interface engineering. *Nat. Commun.* **8**, 1–8 (2017).

21. Wang, N. et al. Perovskite light-emitting diodes based on solution-processed self-organized multiple quantum wells. *Nat. Photon.* **10**, 699–704 (2016).

22. Liu, J., Leng, J., Wu, K., Zhang, J. & Jin, S. Observation of internal photoinduced electron and hole separation in hybrid 2-dimensional perovskite films. *J. Am. Chem. Soc.* **139**, 1432–1435 (2017).

23. Milot, R. L. et al. Charge-carrier dynamics in 2D hybrid metal-halide perovskites. *Nano Lett.* **16**, 7001–7007 (2016).

24. Schlipf, J. & Müller-Buschbaum, P. Structure of Organometal Halide Perovskite Films as Determined with grazing-incidence X-ray scattering methods. *Adv. Energy Mater.* **7**, 1700131 (2017).

25. Kong, W. et al. Characterization of an abnormal photoluminescence behavior upon crystal-phase transition of perovskite $CH_3NH_3PbI_3$. *Phys. Chem. Chem. Phys.* **17**, 16405–16411 (2015).

26. Yamada, Y. et al. Dynamic optical properties of $CH_3NH_3PbI_3$ single crystals as revealed by one- and two-photon excited photoluminescence measurements. *J. Am. Chem. Soc.* **137**, 10456–10459 (2015).

27. Ma, J. & Wang, L. Nanoscale charge localization induced by random orientations of organic molecules in hybrid perovskite $CH_3NH_3PbI_3$. *Nano Lett.* **15**, 248–253 (2014).

28. Stoumpos, C. C. et al. Ruddlesden–Popper hybrid lead iodide perovskite 2D homologous semiconductors. *Chem. Mater.* **28**, 2852–2867 (2016).

29. Moreels, I. et al. Size-dependent optical properties of colloidal PbS quantum dots. *ACS Nano* **3**, 3023–3030 (2009).

30. Wu, X., Trinh, M. T. & Zhu, X. Y. Excitonic many-body interactions in two-dimensional lead iodide perovskite quantum wells. *J. Phys. Chem. C* **119**, 14714–14721 (2015).

31. Leguy, A. M. A. et al. Experimental and theoretical optical properties of methylammonium lead halide perovskites. *Nanoscale* **8**, 6317–6327 (2016).

32. Wang, Y., Suna, A., Mahler, W. & Kasowski, R. PbS in polymers: from molecules to bulk solids. *J. Chem. Phys.* **87**, 7315–7322 (1987).

33. Yang, Y. et al. Observation of a hot-phonon bottleneck in lead-iodide perovskites. *Nat. Photon.* **10**, 53–59 (2015).

34. Jeon, N. J. et al. Solvent engineering for high-performance inorganic–organic hybrid perovskite solar cells. *Nat. Mater.* **13**, 897–903 (2014).

35. Munir, R. et al. Hybrid perovskite thin-film photovoltaics: in situ diagnostics and importance of the precursor solvate phases. *Adv. Mater.* **29**, 1604113 (2017).

36. Rong, Y. et al. Solvent engineering towards controlled grain growth in perovskite planar heterojunction solar cells. *Nanoscale* **7**, 10595–10599 (2015).

37. Barrit, D. et al. Hybrid perovskite solar cells: in situ investigation of solution-processed PbI_2 reveals metastable precursors and a pathway to producing porous thin films. *J. Mater. Res.* **32**, 1899–1907 (2017).

38. Wang, F. et al. Two-dimensional semiconductor nanocrystals: properties, templated formation, and magic-size nanocluster intermediates. *Acc. Chem. Res.* **48**, 13–21 (2014).

39. Liu, Y., Wang, F., Wang, Y., Gibbons, P. C. & Buhro, W. E. Lamellar assembly of cadmium selenide nanoclusters into quantum belts. *J. Am. Chem. Soc.* **133**, 17005–17013 (2011).

40. Morrison, P. J., Loomis, R. A. & Buhro, W. E. Synthesis and growth mechanism of lead sulfide quantum platelets in lamellar mesophase templates. *Chem. Mater.* **26**, 5012–5019 (2014).

41. Reidenger, A. et al. An intrinsic growth instability in isotropic materials leads to quasi-two-dimensional nanoplatelets. *Nat. Mater.* **16**, 743–748 (2017).

42. Yu, L. et al. Programmable and coherent crystallization of semiconductors. *Sci. Adv.* **3**, 1–10 (2017).

43. Park, K. H., Jang, K. & Son, S. U. Synthesis, optical properties, and self-assembly of ultrathin hexagonal In_2S_3 nanoplates. *Angew. Chem. Int. Ed.* **45**, 4608–4612 (2006).

44. Zhang, Y., Sun, X., Si, R., You, L. & Yan, C. Single-crystalline and monodisperse LaF_3 triangular nanoplates from a single-source precursor. *J. Am. Chem. Soc.* **127**, 3260–3261 (2005).

45. Chen, A. Z. et al. Origin of vertical orientation in two-dimensional metal halide perovskites and its effect on photovoltaic performance. *Nat. Commun.* **9**, 1–7 (2018).

46. Lee, E. M. Y. & Tisdale, W. A. Determination of exciton diffusion length by transient photoluminescence quenching and its application to quantum dot films. *J. Phys. Chem. C* **119**, 9005–9015 (2015).

47. Cao, D. H., Stoumpos, C. C., Farha, O. K., Hupp, J. T. & Kanatzidis, M. G. 2D homologous perovskites as light-absorbing materials for solar cell applications. *J. Am. Chem. Soc.* **137**, 7843–7850 (2015).

Author contributions

R.Q.-B. and E.H.S. designed and directed this study. R.Q.-B. prepared the samples. R.Q.-B., A.G.-P., R.M. and Z.Y. carried out the synchrotron X-ray scattering experiments. R.Q.-B. and A.G.-P. performed the analysis of the X-ray scattering data, supported and advised by M.F.T. R.Q.-B. carried out the TA spectroscopy measurements and both R.Q.-B. and A.H.P. performed the analysis of this data. R.Q.-B. and A.H.P. fabricated and tested the solar cells. S.O.K., A.A., M.F.T. and E.H.S. supervised the work. R.Q.-B., A.G.-P., M.F.T. and E.H.S. wrote the manuscript with critical input from all the authors.

Competing interests

The authors declare no competing financial interests.

Additional information

Methods

Material synthesis. Reduced-dimensional $(PEA)_2(MA)_{n-1}Pb_nI_{3n+1}$ perovskite solutions were prepared by dissolving the appropriate stoichiometric quantities of PbI_2, methylammonium iodide and PEA iodide in γ-butyrolactone/DMSO (1:1 volume ratio) or DMF (for hot-cast films) at 70 °C for 1 h with vigorous stirring. The resulting solution was filtered with a PTFE syringe filter (0.2 μm) before deposition. The next step depends on whether spin casting or hot casting is used:

- For spin casting, the solution was then deposited onto the substrate via a consecutive two-step spin-coating process at 1,000 and 5,000 revolutions per minute (r.p.m.) for 10 and 80 s, respectively. Halfway into the second spin step, 200 μl of chlorobenzene was deposited on the substrate. The resulting films were annealed at 70 °C immediately thereafter for 20 min.
- For hot casting, the substrates were heated to 150 °C. The substrate was quickly placed on the spinner, the solution was dropped on to the substrate followed by a one-step spin-coating process at 5,000 r.p.m. for 20 s.

For most films (all the data presented in Figs. 1, 2, 3 and 5), the molarity was chosen so that the films would exhibit commensurate thickness. In this case, 200 nm was identified as a suitable thickness. The molarity required to achieve a 200 nm thickness was found to depend on the target $\langle n \rangle$ (verified by AFM). The amount of precursor to add is determined by the equation:

$$M = \frac{XVA}{\left[M_{PbI_2} + 2\frac{M_{PbI_2}}{\langle n \rangle} + \frac{M_{MAI}(\langle n \rangle - 1)}{\langle n \rangle}\right]}$$

where

$$A = M_{PbI_2} \text{ or } 2\frac{M_{PbI_2}}{\langle n \rangle} \text{ or } \frac{M_{MAI}(\langle n \rangle - 1)}{\langle n \rangle}$$

V is the volume of the solvent and X is a molarity factor. This equation was found to lead to samples of commensurate thickness. X is 1.1, 0.9, 0.5 and 0.3 for spin-cast BTA films, spin-cast PEA films, hot-cast BTA films and hot-cast PEA films, respectively, for films of 200 nm.

Layered perovskite single crystals of $n = 2$, 3 and 4 were synthesized according to previous literature[28]. These are significantly purer than the RDP films, but regions can be found with some mixed n phases. Figure 2d, for instance, was measured on a single crystal grown with the $n = 3$ synthesis.

TA spectroscopy. Femtosecond laser pulses of 1,030 nm generated by a Yb:KGW laser at a 5 kHz repetition rate (Pharos (Light Conversion)), passed through an optical parametric amplifier (Orpheus (Light Conversion)) selected for 480 nm light. The latter served as the pump pulse, whereas the probe pulse was generated by focusing the initial 1,030 nm pulse into a sapphire crystal, which resulted in a white-light continuum (Helios (Ultrafast)). With a temporal resolution of the system of ~350 fs, each time step meant delaying the probe pulse with respect to the pump, with time steps that increased exponentially. Every other pump pulse was blocked with a chopper to determine the change in optical density. After going through a grating spectrograph, the pulses were measured by means of a charge-coupled device (CCD) (Helios (Ultrafast)). Multiple scans were taken for each sample at each power, and the average of these scans was used.

Grazing-incidence X-ray scattering. The RDP GIWAXS data (ex situ and in situ during annealing) were collected at the Stanford Synchrotron Radiation Lightsource. 2D scattering was collected at a 2° incidence with monochromatic 12.7 keV X-rays and recorded on a Rayonix Mx-225 detector that measured 225×225 mm². Samples were measured in a chamber filled with helium. Images were calibrated using LaB6 and integrated to 1D patterns using the Nika software package[48] and the GIXSGUI MATLAB plug-in[49]. In the kinetics analysis, scans were recorded every 20 s. To calculate the intensity of a peak, the region of $Q \pm 0.05 \text{ Å}^{-1}$ around the peak was fit to a linear background and a Voigt profile. The integrated intensity of the Voigt profile was plotted and normalized to the highest intensity of that peak in the measurement.

Additional ex situ GIWAXS measurements were conducted at the Hard X-ray MicroAnalysis (HXMA) beamline of the Canadian Light Source (CLS). An energy of 17.998 keV ($\lambda = 0.6888$ Å) was selected using a Si(111) monochromator. Patterns were collected on a SX165 CCD camera (Rayonix) placed at a distance of 175 mm from the sample. A lead beamstop was used to block the direct beam. Images were calibrated using LaB6 and processed via the Nika software package and the GIXSGUI MATLAB plug-in.

GISAXS data and time-resolved in-situ GIWAXS measurements performed during the spin coating were collected at the D1 beamline of the Cornell High Energy Synchrotron Source (CHESS). A Pilatus 200K detector was employed to record the scattering from the sample. The sample-to-detector distance was set to 815.24 mm and 165.83 mm for GISAXS and GIWAXS measurements, respectively. The incident angle was kept at 0.5° with respect to the sample plane. The wavelength of the X-rays was 0.117 nm. Spin-coating experiments were conducted using a custom-built spin-coating stage that was computer controlled remotely

from outside the hutch, as explained previously[35,37]. The splashing of the solution during spin coating was collected using an X-ray-transparent Kapton splash guard. There was a delay of around 20–30 s between the solution dropping and the start of spin coating and measurement. All these experiments were performed with an exposure time of 0.2 s and in an ambient environment where the relative humidity was around 20–30%.

Additional ex situ GISAXS data were collected at the National Synchrotron Radiation Research Center (NSRRC) in Hsinchu, Taiwan. 2D scattering was collected at a 0.2° incidence, with monochromatic 15 keV X-rays and recorded on a Pilatus detector. The samples were measured in air.

AFM. AFM measurements were performed with an Asylum Research Cypher system. The AFM was operated in an a.c. mode in air to obtain topographical and phase images. Silicon ASYELEC-02 probes with titanium iridium coatings from Asylum Research were used for all the imaging. The probes typically have a spring constant of 42 N m⁻¹.

Computing XRD patterns. XRD patterns and structure factors were computed from Crystallographic Information Files (details in Supplementary Information) by means of 3D atomistic visualization, manipulation and computation software Mercury[50] and VESTA[51].

Perovskite solar cell fabrication. Prepatterned indium tin oxide (TFD Devices) coated glass was cleaned using acetone and then isopropanol. The TiO₂ electron transport layers (ETLs) were spin coated on indium tin oxide substrates from the colloidal TiO₂ nanocrystal solutions at a spin speed of 3,000 r.p.m. for 20 s without ramping, and then annealed on a hotplate at 150 °C for 30 min in air. The TiO₂-coated substrates were then transferred into a nitrogen-filled glovebox for the deposition of perovskite films. Perovskite precursor solutions were prepared by dissolving methylammonium iodide, PEA iodide, butylammonium iodide and lead(II) iodide in a 1:1 mixture of DMSO and γ-butyrolactone. (The ratio of the precursors and concentration depends on the designation of n for the film and the desired thickness. For $n < 10$, concentrations of Pb^{2+} were typically 1.0 M, whereas for $n \geq 10$, concentrations of ~1.6 M were used.) The perovskite films were deposited onto the TiO₂ substrates with two-step spin-coating procedures: the first step was 1,000 r.p.m. for 10 s with an acceleration of 100 r.p.m. s⁻¹. The second step was 5,000 r.p.m. for 60 s with a ramp-up of 1,000 r.p.m. s⁻¹. Chlorobenzene (200 μl) was dropped on the spinning substrate during the second step at 30 s before the end of the procedure. The substrate was then transferred onto a hotplate and annealed at 100 °C for 30 min. After cooling down to room temperature, the hole-transport layer was subsequently deposited on top of the perovskite film by spin coating at 4,000 r.p.m. for 20 s (2,000 r.p.m. ramp) using a chlorobenzene solution that contained 65 mg ml⁻¹ of Spiro-OMeTAD, 20 μl ml⁻¹ of t-butylpyridine, and 70 μl ml⁻¹ of bis(trifluoromethane)sulfonimide lithium salt (170 mg ml⁻¹ in acetonitrile). A 120 nm Au contact was deposited on top of Spiro-OMeTAD layer by electron-beam evaporation in an Angstrom Engineering deposition system.

Solar cell characterization. The current density–voltage (J–V) characteristics were measured using a Keithley 2400 source meter under the illumination of the solar simulator (Class A (Newport)) at a light intensity of 100 mW cm⁻² as checked with a calibrated reference solar cell (Newport). J–V curves were all measured in a nitrogen atmosphere with a scanning rate of 50 mV s⁻¹ (a voltage step of 10 mV and a delay time of 200 ms). Power conversion efficiencies were determined from the J–V curves. The active area was determined by the aperture shade mask (0.049 cm² for small-area devices) placed in front of the solar cell to avoid an overestimation of the photocurrent density. A spectral mismatch factor of one was used for all J–V measurements.

We fabricated and characterized ten solar cell samples of each type (80 samples in total), each with four different devices, which amounted to a total of 320 tested devices.

Data availability

The data that support the plots within this paper are available from the corresponding author upon request.

References

48. Ilavsky, J. Nika: software for two-dimensional data reduction. *J. Appl. Crystallogr.* **45**, 324–328 (2012).
49. Jiang, Z. GIXSGUI: a MATLAB toolbox for grazing-incidence X-ray scattering data visualization and reduction, and indexing of buried three-dimensional periodic nanostructured films. *J. Appl. Crystallogr.* **48**, 917–926 (2015).
50. Macrae, C. F. et al. Mercury CSD 2.0—new features for the visualization and investigation of crystal structures. *J. Appl. Crystallogr.* **41**, 466–470 (2008).
51. Momma, K. & Izumi, F. VESTA 3 for three-dimensional visualization of crystal, volumetric and morphology data. *J. Appl. Crystallogr.* **44**, 1272–1276 (2011).

nature research

Corresponding author(s): **Edward H. Sargent**

Solar Cells Reporting Summary

Nature Research wishes to improve the reproducibility of the work that we publish. This form is intended for publication with all accepted papers reporting the characterization of photovoltaic devices and provides structure for consistency and transparency in reporting. Some list items might not apply to an individual manuscript, but all fields must be completed for clarity.

For further information on Nature Research policies, including our data availability policy, see Authors & Referees.

▶ Experimental design

Please check: are the following details reported in the manuscript?

1. Dimensions

   Area of the tested solar cells
   ☒ Yes Methods – Solar cell characterization
   ☐ No

   Method used to determine the device area
   ☒ Yes Methods – Solar cell characterization
   ☐ No

2. Current-voltage characterization

   Current density-voltage (J-V) plots in both forward and backward direction
   ☒ Yes Figure S29
   ☐ No

   Voltage scan conditions
   For instance: scan direction, speed, dwell times
   ☒ Yes Methods – Solar cell characterization
   ☐ No

   Test environment
   For instance: characterization temperature, in air or in glove box
   ☒ Yes Methods – Solar cell characterization
   ☐ No

   Protocol for preconditioning of the device before its characterization
   ☐ Yes None.
   ☒ No

   Stability of the J-V characteristic
   Verified with time evolution of the maximum power point or with the photocurrent at maximum power point; see ref. 7 for details.
   ☐ Yes No maximum power point data is included, as this is not the focus of our work.
   ☒ No

3. Hysteresis or any other unusual behaviour

   Description of the unusual behaviour observed during the characterization
   ☒ Yes Figure S29
   ☐ No

   Related experimental data
   ☒ Yes Figure S29
   ☐ No

4. Efficiency

   External quantum efficiency (EQE) or incident photons to current efficiency (IPCE)
   ☐ Yes EQE data was not included.
   ☒ No

   A comparison between the integrated response under the standard reference spectrum and the response measure under the simulator
   ☐ Yes Not applicable.
   ☒ No

   For tandem solar cells, the bias illumination and bias voltage used for each subcell
   ☐ Yes Not applicable.
   ☒ No

5. Calibration

   Light source and reference cell or sensor used for the characterization
   ☒ Yes Methods – Solar cell characterization
   ☐ No

   Confirmation that the reference cell was calibrated and certified
   ☒ Yes Methods – Solar cell characterization
   ☐ No

Calculation of spectral mismatch between the reference cell and the devices under test

☒ Yes   Methods – Solar cell characterization
☐ No

6. Mask/aperture

Size of the mask/aperture used during testing

☒ Yes   Methods – Solar cell characterization
☐ No

Variation of the measured short-circuit current density with the mask/aperture area

☐ Yes   No other masks were used.
☒ No

7. Performance certification

Identity of the independent certification laboratory that confirmed the photovoltaic performance

☐ Yes   No independent certification laboratories were used.
☒ No

A copy of any certificate(s)
Provide in Supplementary Information.

☐ Yes   Not applicable.
☒ No

8. Statistics

Number of solar cells tested

☒ Yes   Methods – Solar cell characterization
☐ No

Statistical analysis of the device performance

☐ Yes   An in-depth statistical analysis of performance was not included.
☒ No

9. Long-term stability analysis

Type of analysis, bias conditions and environmental conditions
For instance: illumination type, temperature, atmosphere humidity, encapsulation method, preconditioning temperature

☐ Yes   The stability of the devices was not the focus of our work.
☒ No   That being stated, we measured the performance of devices after multiple days of exposure to air and found negligible variations in the performance.